THE ASTROPHYSICAL JOURNAL, 486:484–501, 1997 September 1

SOLAR INTERFACE DYNAMOS. I. LINEAR, KINEMATIC MODELS IN CARTESIAN GEOMETRY

K. B. MACGREGOR AND P. CHARBONNEAU
High Altitude Observatory, National Center for Atmospheric Research,[1] P.O. Box 3000, Boulder, CO 80307-3000;
mac@hao.ucar.edu, paulchar@hao.ucar.edu
Received 1996 August 9; accepted 1997 March 27

ABSTRACT

We describe a simple, kinematic model for a dynamo operating in the vicinity of the interface between the convective and radiative portions of the solar interior. The model dynamo resides within a Cartesian domain, partioned into an upper, convective half and lower, radiative half, with the magnetic diffusivity η of the former region (η_2) assumed to exceed that of the latter (η_1). The fluid motions that constitute the α-effect are confined to a thin, horizontal layer located entirely within the convective half of the domain; the vertical shear is nonzero only within a second, nonoverlapping layer contained inside the radiative half of the domain. We derive and solve a dispersion relation that describes horizontally propagating dynamo waves. For sufficiently large values of a parameter analogous to the dynamo number of conventional models, growing modes can be found for any ratio of the upper and lower magnetic diffusivities. However, unlike kinematic models in which the shear and α-effect are uniformly distributed throughout the same volume, the present model has wavelike solutions that grow in time only for a finite range of horizontal wavenumbers.

An additional consequence of the assumed dynamo spatial structure is that the strength of the azimuthal magnetic field at the location of the α-effect layer is reduced relative to the azimuthal field strength at the shear layer. When the jump in η occurs close to the α-effect layer, it is found that over one period of the dynamo's operation, the ratio of the maximum strengths of the azimuthal fields at these two positions can vary as the ratio (η_1/η_2) of the magnetic diffusivities.

Subject headings: MHD — methods: analytical — Sun: interior — Sun: magnetic fields

1. INTRODUCTION

One of the principal goals of solar physics is to obtain a quantitative understanding of the origin and nature of the activity which is observed to occur throughout the Sun's surface layers and atmosphere. A notable achievement of solar physics during the past two decades has been the recognition of the fact that there is a close relationship between such activity and magnetism. The Sun's magnetic field not only structures emitting regions within the atmosphere but also apparently contributes to their energy balance. It does so by guiding and/or storing mechanical energy from deeper atmospheric layers, and by direct heating through the rapid dissipation of magnetic energy at sites of field line reconnection (see, e.g., Parker 1994a, and references therein).

The time-dependent magnetic field of the Sun is presumably the product of a hydromagnetic dynamo. According to the description provided by mean-field electrodynamics (see § 2 below), rotation is of crucial importance to the operation of the solar dynamo. The shear flow field that results from the internal differential rotation of the Sun allows for the inductive conversion of poloidal magnetic fields to toroidal magnetic fields. Through the action of the Coriolis force, the overall solar rotation endows the near-radial fluid motions associated with convection and convective overshoot with the helicity required to regenerate poloidal fields from toroidal fields (the so-called α-effect). Together these complementary magnetohydrodynamical (MHD) processes comprise the dynamo mechanism thought to be responsible for the observed behavior of the Sun's magnetic field over the course of the 22 yr solar magnetic activity cycle.

Although the precise position of the dynamo domain within the Sun is uncertain, several independent lines of evidence now point to a location immediately below the interface between the convective and radiative portions of the solar interior ($r \approx 0.70\ R_\odot$). Some of the support for this hypothesis comes from the interpretation of helioseismological observations that pertain to the rotational state of the outer 25%–30% of the Sun's radius (see, e.g., Brown et al. 1989; Gough 1991 and references therein). Among other things, measurements and analyses of *p*-mode frequency splittings indicate that the pattern of differential rotation with latitude deduced from observations of the solar surface persists along radii to the bottom of the convection zone. Just beneath the base of the convective envelope, the angular velocity of material at polar latitudes increases slightly with depth, while that of equatorial material undergoes a decrease of similar magnitude. At still greater depths, the angular velocities of the poles and equator approach a common value; by the time a depth $r \approx 0.65\ R_\odot$ has been attained, uniform rotation at a rate intermediate between the surface rotation of these regions prevails (Tomczyk, Schou, & Thompson 1995). Hence, it would appear that only within a narrow layer (thickness $\lesssim 0.1\ R_\odot$) in the vicinity of the interface does the radial gradient of the angular velocity Ω have a value different from zero (see, e.g., Gillman, Morrow, & DeLuca 1989). Since the shearing motions implied by this quantity contribute to the production of toroidal field from poloidal field, it must be concluded that at least some portion of the dynamo domain lies within the shell-like volume having $\partial\Omega/\partial r \neq 0$.

An additional indication that the dynamo might be situated in the stable, overshoot region underlying the convection zone is derived from studies of bipolar magnetic regions (BMRs) in the photospheric layers of the Sun. It is

[1] The National Center for Atmospheric Research is sponsored by the National Science Foundation.

generaly believed that such features represent looplike upwellings through the visible solar surface of otherwise submerged, primarily azimuthally directed magnetic fields (see, e.g., Parker 1994b). If the origin of these flux tubes is the shearing layer located near the bottom of the convection zone, then their principal means of transport to the photosphere is magnetic buoyancy. In this regard, recent work (Fan, Fisher, & DeLuca 1993; D'Silva 1993; D'Silva & Choudhuri 1993; D'Silva & Howard 1994; Caligari, Moreno-Insertis, & Schüssler 1995; Fan & Fisher 1996) has shown that the observed behaviors of BMR emergence latitudes and tilts (i.e., the angle between the line joining the magnetic footpoints of the bipole and the latitude of emergence), when interpreted in light of models for buoyantly rising flux tubes, provide tight constraints on the strength of azimuthal fields in the vicinity of the dynamo region. For fields smaller than about 6×10^4 G, the dynamical state of a buoyant flux bundle is dominated by the Coriolis force, leading to tube motion which is preferentially parallel to the Sun's rotation axis, and eruption at high latitudes with tilts that are not in agreement with observations. Alternatively, if the field is stronger than about 1.6×10^5 G, the dominance of the magnetic bouyancy force leads to flux tube motion in the radial direction, but permits only Coriolis-produced tilts that are smaller in magnitude than observed values. Taken together, then, these results suggest that reasonable accord with observations can be achieved if the strength of the azimuthal field at the convection zone base is of the order of 10^5 G.

The retention and amplification of such strong fields is problematical if the solar dynamo functions entirely within the nearly adiabatically stratified convection zone. It is well known (see, e.g., Parker 1975) that a flux tube immersed in this environment would be brought to the surface of the Sun by magnetic buoyancy in a time that is far shorter than the duration of the solar cycle. However, detailed investigations of the dynamical stability of toroidal flux distributions inside the Sun indicate that fields with strengths as high as 10^5 G can be stored within the subadiabatic overshoot layer for periods of time much longer than the length of the solar cycle (Schüssler et al. 1994). In view of this, it might be anticipated that a physically consistent, thin-layer dynamo model could be developed in which the small-scale effects required to regenerate the mean magnetic field are supplied by the helical fluid motions associated with overshooting convective elements. Yet a fundamental obstacle which must be surmounted in pursuit of this objective is the fact that the inferred azimuthal field strengths of 10^5 G are more than an order of magnitude greater than equipartition values based on the kinetic energy of the turbulent convective fluid motions (Parker 1993). As a result, they must impede the turbulent flows that give rise to the α-effect and enhanced resistive diffusion, and thereby hinder the operation of the dynamo.

These difficulties have their origin in the presumption that the generation of strong toroidal fields by fluid shear and the creation of new poloidal fields by the α-effect take place within the same region. As noted by Parker (1993), this situation can be circumvented by considering an *interface* dynamo in which the large-scale shear and α-effect occupy separate and distinct portions of the domain. The evidence summarized in the preceding paragraphs lends credibility to such a representation, suggesting that the site of azimuthal field production is below the core-envelope interface while the α-effect is confined to the region above. For a dynamo configured in this way, Parker (1993) showed that the ratio of the maximum values of the azimuthal fields in the two regions varies inversely as the square root of the ratio of their respective magnetic diffusivities. Since the diffusivity of material located above the interface is likely to be greater than that of the material below, the magnitude of the azimuthal field in the upper region is reduced relative to that of the field in the lower region. Because of this behavior, for suitably chosen diffusivity ratios, it is possible to construct solutions with strong azimuthal fields below the interface and subequipartition azimuthal fields above.

In the present paper, we study the properties of another such dynamo model, one in which the component physical processes are relegated to respective halves of a Cartesian domain that is partitioned by a surface the location of which coincides with the convection zone bottom. Beneath this surface, the assumed presence of a shear flow in the stably stratified material leads to the existence of a significant azimuthal field (i.e., a magnetic field component in the flow direction), along with a commensurably reduced magnetic diffusivity and a strongly inhibited α-effect. Above the surface, the absence of a shear in the convectively unstable fluid medium implies normal operation of the α-effect, a substantial turbulent contribution to the diffusivity, and a weak azimuthal magnetic field component. The theoretical and computational aspects of the model are described in § 2, as are the specific parameterizations adopted for the distributions of shear, α-effect, and magnetic diffusivity within the dynamo region. Our model differs from that of Parker (1993) in that the first two of these quantities are not uniform inside their respective halves of the domain, but instead are strongly concentrated in the neighborhood of the interface. Such a modification of Parker's model is motivated by recent analyses of helioseismic observations indicating that the radial gradient of the internal solar angular velocity is nonzero only within a thin layer located *below* the bottom of the convection zone (Kosovichev 1996; Charbonneau et al. 1997). This result suggests that the production of a toroidal field component by the action of a shear flow occurs in a location that is separated from the site of poloidal field regeneration by the α-effect. The dynamo dispersion relation is presented and solved in § 3, and the physical properties of propagating wave modes corresponding to a wide range of input parameter values are discussed. In § 4, we describe the temporal and spatial evolution of the field amplitudes of oscillatory dynamo wave solutions, obtained for a case in which the upper and lower portions of the dynamo domain are characterized by magnetic diffusivities with very different magnitudes. In the concluding section of the paper (§ 5), we discuss the application of these results to the interpretation of the inferred properties of the solar dynamo.

2. MODEL

As discussed in the preceding section, we seek a quantitative description of a hydromagnetic dynamo, operating in the vicinity of the interface between the bottom of the solar convective envelope and the underlying radiative interior. For simplicity, we assume that such a description can be formulated within the framework of mean-field electrodynamics and restrict our attention to a kinematic dynamo of the $\alpha\omega$-type (see, e.g., Moffatt 1978; Parker 1979, and references therein; Stix 1989). Because of turbulent contri-

butions to the transport properties of the material in convectively unstable regions, we anticipate that the fluid layers located above and below the interfacial surface will be characterized by magnetic diffusivities with quite different magnitudes. Moreover, for the reasons presented in § 1, we do *not* consider a dynamo in which the α-effect and fluid velocity shear are co-spatial and uniformly distributed throughout the domain. Instead, we suppose that the generation of toroidal field by differential rotation and the generation of poloidal field by the α-effect take place in separate, distinct portions of the domain. In view of these considerations, and in an effort to keep the subsequent analysis tractable while retaining as much of the essential physics as possible, we adopt the model depicted schematically in Figure 1.

The task of determining the operating modes of the dynamo is simplified considerably if a two-dimensional, retangular slab is the appropriate geometrical description of the dynamo domain. In the Sun, such an approximation is justified if the processes contributing to the functioning of the dynamo are spatially confined to a thin layer the radial extent of which about the interface is small compared to the radius of the interface itself. We assume this to be the case, and erect a local Cartesian coordinate system (x, y, z) with axes oriented in such a way that the directions of increasing x, y, and z coincide with the directions in which the spherical polar coordinates θ, ϕ, and r, respectively, increase (see Fig. 1). The mean, large-scale magnetic field is taken to be independent of the coordinate y (i.e., axisymmetric), and is conveniently represented as the sum of a poloidal component

$$\boldsymbol{B}_P = B_x(x, z, t)\boldsymbol{e}_x + B_z(x, z, t)\boldsymbol{e}_z \,, \tag{1}$$

and a toroidal component

$$\boldsymbol{B}_T = B(x, z, t)\boldsymbol{e}_y \,. \tag{2}$$

In equations (1) and (2), the time (t) dependence of the field components has been explicitly noted, and the quantities $\boldsymbol{e}_x$, $\boldsymbol{e}_y$, and $\boldsymbol{e}_z$ are unit vectors that point along the x-, y-, and z-axes. The poloidal magnetic field component is further derivable from a vector potential

$$\boldsymbol{A} = A(x, z, t)\boldsymbol{e}_y \,, \tag{3}$$

by taking the curl,

$$\boldsymbol{B}_P = \nabla \times \boldsymbol{A} = -\frac{\partial A(x, z, t)}{\partial z}\,\boldsymbol{e}_x + \frac{\partial A(x, z, t)}{\partial x}\,\boldsymbol{e}_z \,. \tag{4}$$

The prescriptions given in equations (2) and (4) ensure that the condition $\nabla \cdot (\boldsymbol{B}_P + \boldsymbol{B}_T) = 0$ is fulfilled everywhere within the domain.

In the Sun, internal differential rotation is thought to be the primary means for converting poloidal fields into toroidal fields. Hence, among the additional quantities which must be supplied in order to complete the model is the large-scale fluid velocity field $\boldsymbol{u}$ within the dynamo region. Given the kinematic nature of the model considered herein, this flow field is a specified quantity. In the present application, we presume that $\boldsymbol{u}$ is independent of both time and latitude (i.e., the coordinate x), and so can be written in the form

$$\boldsymbol{u} = u(z)\boldsymbol{e}_y \,. \tag{5}$$

Using equations (2), (4), and (5), the mean-field induction equation (see Moffatt 1978) can be separated into poloidal and toroidal components, a procedure which yields two equations governing the temporal and spatial evolution of the vector potential (A) and the y-component of the magnetic field (B). These dynamo equations are

$$\frac{\partial A}{\partial t} = \eta\left(\frac{\partial^2}{\partial x^2} + \frac{\partial^2}{\partial z^2}\right)A + \alpha B \,, \tag{6}$$

and

$$\frac{\partial B}{\partial t} = \eta\left(\frac{\partial^2}{\partial x^2} + \frac{\partial^2}{\partial z^2}\right)B + \frac{\partial u}{\partial z}\frac{\partial A}{\partial x} + \frac{\partial \eta}{\partial z}\frac{\partial B}{\partial z} \,, \tag{7}$$

where the magnetic diffusivity η (in $\mathrm{cm^2\ s^{-1}}$) is related to the electrical conductivity σ_{el} of the plasma according to $\eta = c^2/(4\pi\sigma_{\mathrm{el}})$, and includes contributions from both microscopic collisional processes and turbulent transport. In addition, the quantity α (in $\mathrm{cm\ s^{-1}}$) appearing in equation (6) describes the way in which the large-scale poloidal field is regenerated from toroidal field by the helical fluid motions associated with turbulent convection in the rotating Sun (the α-effect). We regard α, η, and the velocity shear $\partial u/\partial z$ as quantities whose magnitudes and functional forms can be freely specified. For the computations to be reported on in the present paper, we chose the particular representations

$$\eta = \eta_1 + (\eta_2 - \eta_1)\theta(z - h) \,, \tag{8}$$

$$\alpha = \gamma_0\,\delta(z - d) \,, \tag{9}$$

$$\frac{\partial u}{\partial z} = \omega_0\,\delta(z) \,, \tag{10}$$

where $\theta(z)$ and $\delta(z)$ are, respectively, the unit step function and delta function, and η_1, η_2, γ_0 (in $\mathrm{cm^2\ s^{-1}}$), and ω_0 (in $\mathrm{cm\ s^{-1}}$) are constants. Note that due to the presence of delta functions in equations (9) and (10), γ_0 and ω_0 differ dimensionally from the corresponding α-effect and shear coefficients of conventional mean-field dynamo equations.

With the coordinate system positioned as indicated in Figure 1, the transition between the radiative and convective portions of the interior occurs at $z = h$ ($0 \le h \le d$), at which location the magnetic diffusivity is assumed to increase from the collisional value η_1 to the enhanced, turbulent value η_2. Furthermore, the respective processes of poloidal and toroidal magnetic field generation (i.e., the α-effect and velocity shear) are taken to be concentrated in two distinct layers, the former at $z = d$ in the convective portion of the domain and the latter at $z = 0$ in the radiative region. The velocity distribution $u(z)$ corresponding to the shear given in equation (10) is one in which the regions $z < 0$ and $z > 0$ each move rigidly in the y-direction but with different speeds. Similar dynamo model have been considered by Moffatt (1978) and Kleeorin & Ruzmaikin (1981) in Cartesian geometry, and by Deinzer & Stix (1971) in spherical geometry, although both for the case of a spatially uniform magnetic diffusivity.

The specific choices for α, η, and $\partial u/\partial z$ given in equations (8)–(10) imply that except at the locations $z = 0$, $z = h$, and $z = d$, the dynamo equations (6) and (7) reduce to ordinary diffusion equations. Solutions to this system are uniquely determined through the imposition of boundary and continuity conditions. As will be described in more detail in §§ 3 and 4, we seek solutions A and B that have the form of propagating waves in the x-direction, and whose structure

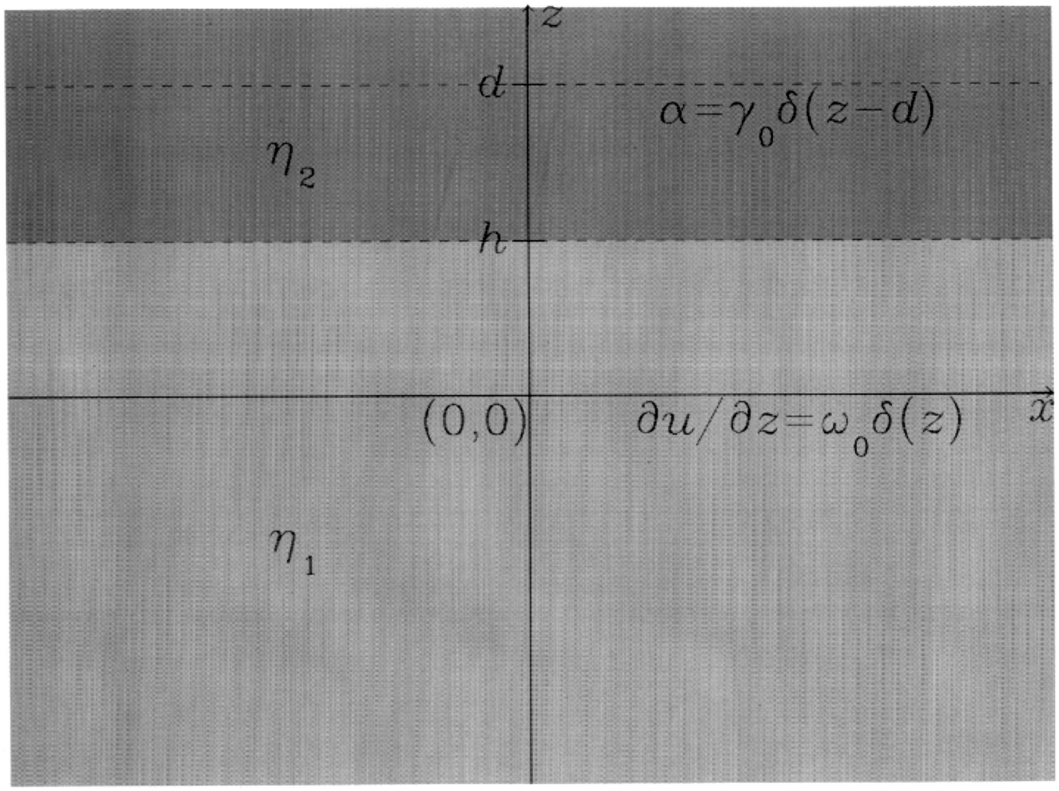

FIG. 1.—Schematic representation of the dynamo model described in § 2 of the text. The magnetic diffusivity has the constant values η_1 in the region $z \leq h$ and η_2 for $z > h$. The vertical shear and α-effect each vanish everywhere except in the two xy-planes that intercept the z-axis at $z = 0$ and $z = d$, respectively.

in the z-direction reflects the vertical structure of the sources of poloidal and toroidal fields. Because these sources are confined to a finite layer ($0 \leq z \leq d$) embedded within material having $\eta \neq 0$, we require that both A and B approach zero as z approaches $\pm\infty$. In addition, we must ensure that as any source surface is crossed, the fields A and B obey physically reasonable continuity conditions and satisfy the complete dynamo equations (6) and (7). At $z = 0$, these considerations lead to the constraining relations

$$[A] = [B] = 0 , \tag{11a}$$

$$\left[\frac{\partial A}{\partial z}\right] = 0 , \tag{11b}$$

and

$$\eta_1\left[\frac{\partial B}{\partial z}\right] = -\omega_0 \frac{\partial A(x, 0, t)}{\partial x} , \tag{11c}$$

when $h > 0$, or

$$\left[\eta \frac{\partial B}{\partial z}\right] = -\omega_0 \frac{\partial A(x, 0, t)}{\partial x} , \tag{11d}$$

when $h = 0$. For a quantity $Q(x, z, t)$, the bracket notation appearing in equations (11) and subsequently represents the limit

$$[Q] = \lim_{\epsilon \to 0} [Q(x, \zeta + \epsilon, t) - Q(x, \zeta - \epsilon, t)] , \tag{12}$$

where $z = \zeta$ can be any of the locations $z = 0$, h, or d. Relations (11a) and (11b) guarantee that the normal and tangential components of the magnetic field are continuous across the shear layer at $z = 0$ (see, e.g., Stratton 1941; Roberts 1967). Expression (11c) or (11d) relates the flux of y-directed field at $z = 0$ to the rate at which z-directed field is sheared there. It is obtained by integrating equation (7) over the interval $-\epsilon \leq z \leq \epsilon$, taking the limit prescribed in equation (12), and using relations (11a) and (11b).

Continuity conditions analogous to those given in equations (11a)–(11d) can also be derived to accommodate the discontinuities at $z = h$ and d indicated by the forms adopted for η and α. At $z = h$ ($\neq 0$ or d), the absence of a surface current implies that the normal and tangential magnetic field components are continuous, so that conditions identical to equations (11a) and (11b) apply at that location. Similarly, integration of equation (7) over the interval $(h - \epsilon) \leq z \leq (h + \epsilon)$ yields the relation

$$\left[\eta \frac{\partial B}{\partial z}\right] = 0 , \tag{13}$$

expressing the fact that the diffusive flux of toroidal field across the surface at $z = h$ is constant despite the different values of η that prevail on either side. At $z = d$, the concentration of the α-effect and its role in the production of poloidal field means that not all field components are continuous there. In particular, although the y- and z-components of the magnetic field are continuous across the α-effect layer, the x-component is not. As a result, equation (11a) holds at $z = d$, while equation (11b) is replaced by either

$$\eta_2\left[\frac{\partial A}{\partial z}\right] = -\gamma_0 B(x, d, t) , \tag{14a}$$

for $h < d$, or

$$\frac{1}{2}(\eta_1 + \eta_2)\left[\frac{\partial A}{\partial z}\right] = -\gamma_0 B(x, d, t) , \tag{14b}$$

for $h = d$, obtained by integrating equation (6) over the interval $(d - \epsilon) \leq z \leq (d + \epsilon)$. Likewise, integration of equation (7) over the same interval leads to the condition

$$\left[\frac{\partial B}{\partial z}\right] = 0 , \tag{15}$$

when $h < d$, or to equation (13) for the case $h = d$. It is readily verified that solutions for A and B obeying the constraints given by expressions (11)–(15) identically satisfy the dynamo equations (6) and (7) at the singular locations $z = 0$, h, and d.

3. DISPERSION RELATION AND DYNAMO MODES

In the present section, the properties of the dynamo model presented in § 1 are studied by deriving solutions to equations (6) and (7) that have the physical character of plane waves traveling in the x-direction. To accomplish this goal, we suppose that within any subdomain (i.e., any of the regions $z < 0$, $0 < z < h$, $h < z < d$, or $z > d$, each with $-\infty < x < \infty$), the fields A and B can be written in the form

$$\begin{bmatrix} A(x, z, t) \\ B(x, z, t) \end{bmatrix} = \begin{bmatrix} a_j(z) \\ b_j(z) \end{bmatrix} \exp\left[\sigma t + i(kx + \omega)\right] , \tag{16}$$

where the growth rate σ, wave vector k (>0), and angular frequency ω are all real constants. The subscript j ($=1, 2$) appearing on the right-hand side of equation (16) accounts for the fact that the solutions must depend upon the magnetic diffusivity, a quantity whose value is η_1 for $z < h$ and η_2 for $z > h$ (see Fig. 1 and eq. [8]). Substituting these assumed solutions into the dynamo equations leads to two ordinary differential equations for the unknown functions $a_j(z)$ and $b_j(z)$. Because of their linearity, these equations are easily solved, yielding

$$\begin{bmatrix} a_j(z) \\ b_j(z) \end{bmatrix} \propto \exp\left(\pm q_j z\right) , \tag{17}$$

where q_j is the complex quantity defined by

$$q_j^2 = k^2 + \frac{(\sigma + i\omega)}{\eta_j} . \tag{18}$$

Complete solutions for A and B are assembled by joining together the component solutions applicable in individual subdomains, and enforcing appropriate boundary conditions at $z = \pm\infty$. In view of equations (16)–(18) and the discussion of § 2, the latter requirement is fulfilled by ensuring that the sign of the real part of q_j is such that the solutions decay as z tends toward $\pm\infty$. The former task is carried out by using the continuity conditions of § 2 to connect the component solutions at the locations $z = 0$, h, and d. As a result of imposing these constraints, a system of linear relations among the complex constant amplitudes characterizing the solutions is obtained. The dynamo dispersion relation is then derived in the course of solving for the individual amplitudes. The details of this straightforward (but tedious) procedure are given in Appendix A; here, we simply present the final result of the calculation, specifically

$$\eta_2(q_1 + q_2)(\eta_1 q_1 + \eta_2 q_2) \times \exp\left[2q_1 h + 2q_2(d - h)\right] = ik\omega_0\gamma_0 , \tag{19a}$$

when $0 \leq h < d$, or

$$\tfrac{1}{2}(\eta_1 + \eta_2)(q_1 + q_2)(\eta_1 q_1 + \eta_2 q_2) \exp\left(2q_1 d\right) = ik\omega_0\gamma_0 , \tag{19b}$$

when $h = d$. The dispersion relations of equations (19a) and (19b) reduce to that given by Moffatt (1978) when the limit $\eta_1 \to \eta_2$, $q_1 \to q_2$ is taken.

Either of the dispersion relations given above is a complex, transcendental equation which, for specified values of η_1, η_2, h, d, ω_0, γ_0, and k, can be solved to determine the growth rate σ and frequency ω of the dynamo. Toward this end, it is convenient to define the dimensionless quantities

$$\begin{aligned} n &\equiv \eta_1/\eta_2 , \quad \kappa \equiv 2kd , \quad \Delta \equiv h/d , \\ v &\equiv \omega_0\gamma_0/(\eta_2^2 k) \quad \text{for} \quad h < d , \\ v &\equiv 2\omega_0\gamma_0/[\eta_2(\eta_1 + \eta_2)k] \quad \text{for} \quad h = d , \end{aligned} \tag{20}$$

and to rewrite q_1^2 and q_2^2 (see eq. [18]) as

$$q_1^2 = k^2(1 + s) , \quad q_2^2 = k^2(1 + ns) , \tag{21}$$

with

$$s = s_r + is_i \equiv \left(\frac{\sigma}{\eta_1 k^2}\right) + i\left(\frac{\omega}{\eta_1 k^2}\right) . \tag{22}$$

Using these definitions, equations (19a) and (19b) both assume the general form

$$1 + n(1 + 2s) + (n + 1)\sqrt{(1 + s)(1 + ns)} - iv \exp\left\{-\kappa[\Delta\sqrt{(1 + s)} + (1 - \Delta)\sqrt{(1 + ns)}]\right\} = 0 , \tag{23}$$

where positive square roots have been taken throughout. Note that if $0 \leq \Delta < 1$, the quantity v appearing in equation (23) is given by the first such definition among the relations (20), while for $\Delta = 1$, the second definition applies; the definitions are identical for the case in which $n = 1$.

The left-hand side of equation (23), when considered as a function of the complex variable s, is multivalued because of the three square roots present therein. To uniquely define each of these functions (and therefore eq. [23] as a whole), it is necessary to cut the s-plane and thereby remove any potential for ambiguity. Consider a dynamo or other linear problem whose mathematical formulation is similar to the one described above, except that it is to be solved as an initial value problem for $t > 0$ using Laplace transform techniques. An appropriate contour in the complex plane for calculating the inversion integral could be constructed by joining the ends of a semicircular arc in the left-half plane with a vertical line having a constant, positive real part (see, e.g., Mathews & Walker 1970). In the event that the integrand contained a branch point or points, such singularities could be treated by introducing a branch cut along the negative real axis and deforming the contour as required in its vicinity. In the present application, we proceed by analogy with this hypothetical example and cut the s-plane along the negative s_r-axis. More specifically, for each of the square roots appearing in equation (23) in turn, we define branch cuts along $s_r < 0$ extending (1) between the two branch points at $s = -1$ and $s = -1/n$, (2) from $s = -1$ to $s = -\infty$, and from $s = -1/n$ to $s = -\infty$.

Having adopted these conventions, the analysis proceeds by separating the dispersion relation given by equation (23) into real and imaginary parts. The two equations that result from this operation can then be solved simultaneously to obtain the roots s_r and s_i. Because of their complexity, these equations must be solved by numerical means. The results described in this and subsequent sections were derived using a standard Newton-Raphson method for refining an initial guess at the solution to a system of nonlinear equations. An alternative approach to solving the dynamo dispersion is to apply the Newton-Raphson method directly to equation (23) alone rather than to the two equations corresponding to its real and imaginary parts. In this case, FORTRAN-supplied utilities for performing arithmetic operations on complex numbers and evaluating functions of complex variables can be used to compute the complex-valued functions represented by equation (23) and its derivative. We have compared the performance of these two techniques by using them to solve the dispersion relation (23) for the case $n = 1$. Although the latter method was found to be somewhat faster and more efficient computationally, both solution strategies yielded identical numerical results.

In Figure 2, we show the quantities $s_r \equiv (\sigma/\eta_1 k^2)$ (*dashed lines*) and $s_i \equiv (\omega/\eta_1 k^2)$ (*solid lines*) as functions of $\kappa \equiv 2kd$ for a dynamo model with uniform magnetic diffusivity [$n \equiv (\eta_1/\eta_2) = 1$]. Along each of the curves in Figure 2, the parameter v has a constant value; for the curves labeled *a*, *b*, *c*, and *d*, $v = 10$, 20, 30, and 40, respectively, while for those labeled *a*′, *b*′, *c*′, and *d*′, $v = -10$, -20, -30, and -40. In interpreting the computational results depicted Figures 2–4, we choose to regard the values of ω_0, d, η_1 and η_2 as fixed. Consequently, the respective variations of s_r and s_i as functions of κ reflect the dependence of those quantities on the wave vector k. Likewise, the assumed constancy of v along curves spanning a range of κ values requires that the k-dependence of this quantity (see eq. [20]) be compensated for by a corresponding variation in the magnitude of γ_0 (i.e., in the strength of the α-effect). The dimensionless number v assumes a role analogous to that played by the dynamo number in conventional kinematic $\alpha\omega$-dynamo models (see Moffatt 1978; Parker 1979), in that it provides a measure of the extent to which the combined efforts of the α-effect and large-scale shear are successful in maintaining the field against resistive decay.

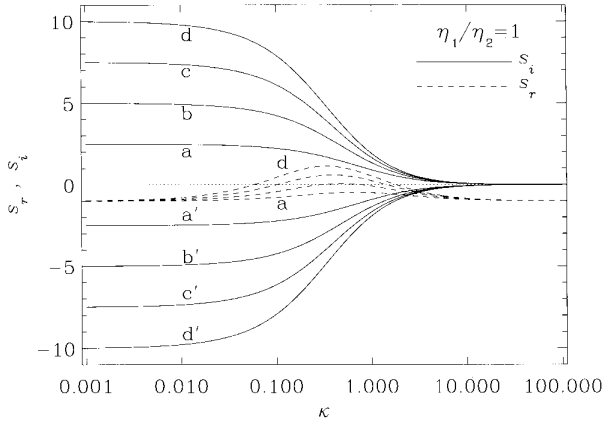

FIG. 2.—Real and imaginary parts, $s_r = \sigma/(\eta_1 k^2)$ and $s_i = \omega/(\eta_1 k^2)$, of roots to the dispersion relation (eq. [23]) as functions of $\kappa = 2kd$ for a dynamo with $n = (\eta_1/\eta_2) = 1$. The parameter v is constant along each curve, having the values 10, 20, 30, and 40 for those labeled a, b, c, and d, and the values -10, -20, -30, and -40 for those labeled a′, b′, c′, and d′.

As is evident from Figure 2, for fixed κ: (1) the magnitudes $|s_i|$ of the imaginary parts of the roots of the dispersion relation depend on the magnitude of v but not on the sign; (2) the sign of s_i is the same as the sign of v; and (3), the magnitudes and signs of the real parts s_r of the solutions corresponding to v and $-v$ are identical. Since it has been assumed that $k > 0$ throughout (see eq. [16] and discussion thereof), solutions with $s_i > 0$ represent plane dynamo waves propagating in the direction $-\boldsymbol{e}_x$, while solutions having $s_i < 0$ represent waves propagating in the direction $+\boldsymbol{e}_x$. In view of the fact that the only distinction between the two sets of modes is their direction of propagation, we henceforth (for simplicity) restrict our attention to just those waves for which both v and s_i are > 0. Note that for $\kappa \ll 1$, s_i exhibits little (if any) dependence on κ, and varies nearly linearly with v. In units of the diffusion time (d^2/η_1) between the two layers in which α and $\partial u/\partial z$ are, respectively, nonzero, the period of the dynamo wave is $8\pi/(\kappa^2 s_i)$. For the solutions shown in Figure 2, this number is $\sim 10^6$–10^7 for $\kappa \approx 10^{-3}$, indicating that dynamo action is extremely weak for modes having very long wavelengths $\lambda[=(2\pi/k) \gg d]$. Indeed, in this regime, the magnitude of γ_0 is insufficient to sustain the field through the regenerative α-effect. Consequently, for the entire range of v values used to construct the graph, the waves have $s_r \approx -1$ and are damped in a time (in units of d^2/η_1) $\sim 4/\kappa^2$.

These results can be validated by comparison with analytic solutions for s_r and s_i, obtained by considering several approximate representations of the dynamo dispersion relation that apply when certain parameters have suitably small values. For example, when κ is sufficiently small that the exponential appearing in equation (23) can be replaced by unity, the dispersion relation becomes (after some manipulation)

$$\left[\left(\frac{2n}{n+1}\right)^2 - n\right]s^2 - \left[\left(\frac{4n}{n+1}\right)\left(\frac{iv}{n+1} - 1\right) + n + 1\right]s + \left[\left(\frac{iv}{n+1} - 1\right)^2 - 1\right] = 0 . \quad (24)$$

For the case in which the dynamo domain is characterized by a single value of the magnetic diffusivity (i.e., $n = 1$), it is easily seen that equation (24) further reduces to the linear relation

$$s = -1 + i\frac{v}{4}, \quad (25)$$

in agreement with the numerical results presented above. Note that for finite values of k, equation (25) describes the behavior of an $n = 1$ dynamo in which the shear and α-effect layers are coincident (i.e., $d = 0$). Clearly in such a situation no growing mode ($s_r > 0$) can exist, a behavior already observed by Deinzer & Stix (1971) in their spherical solutions.

For somewhat larger values of κ, the dispersion relation canot be so simply approximated. Retention of the first two terms in the series expansion for the exponential function in equation (23) leads to

$$1 + s - i\frac{v}{4} = -i\frac{\kappa v}{4}\sqrt{1+s}, \quad (26)$$

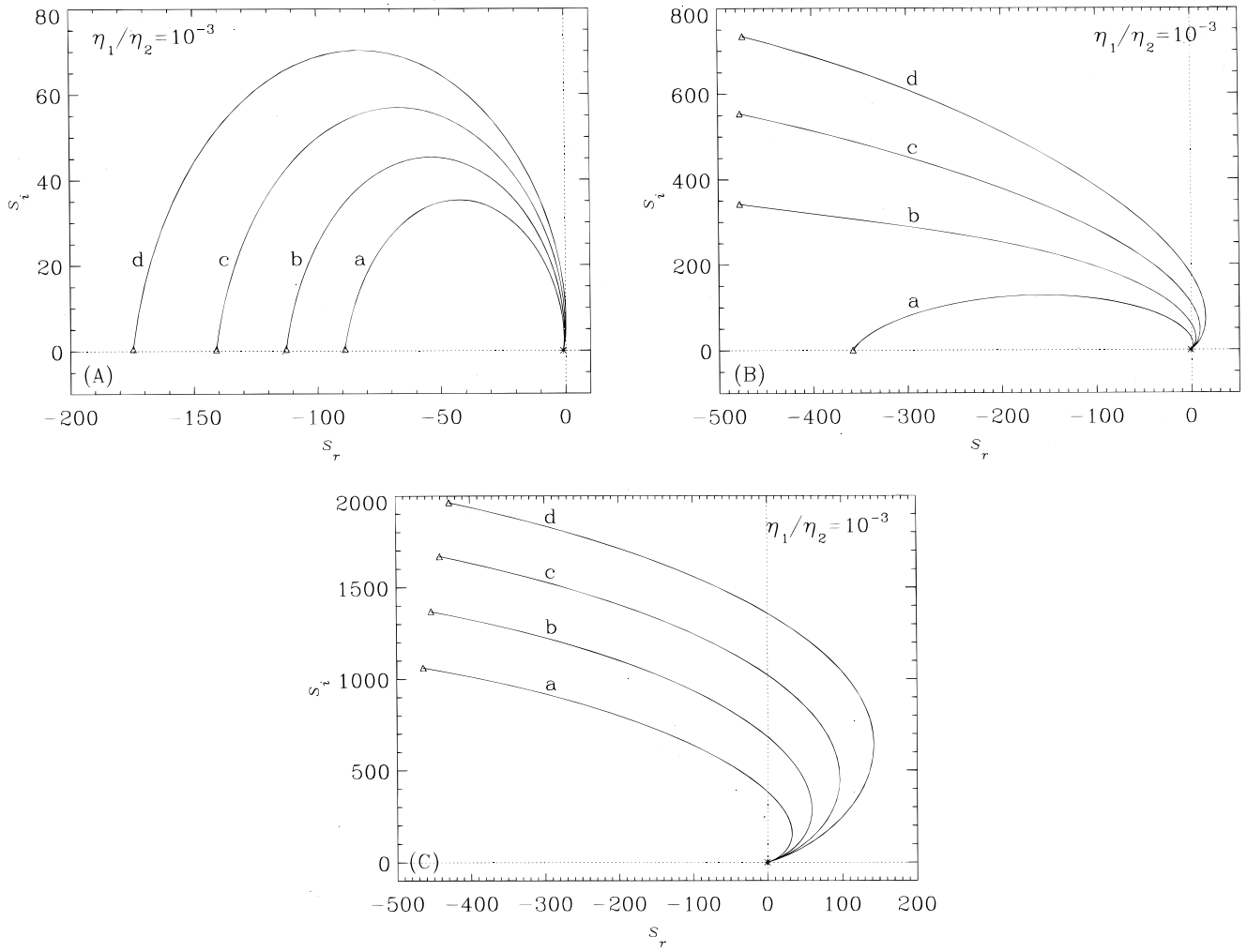

FIG. 3.—Quantities s_r and s_i depicted in the complex s-plane for a dynamo model with $n = 10^{-3}$ and $\Delta = 1$, as described in the text. The triangles mark the small-κ end of each solution locus. The curves labeled a, b, c, and d, were obtained for $v = 9$, 10, 11, and 12. (*b*) s_r and s_i for the same model but with $v = 15.16$ (*a*), 20 (*b*), 25 (*c*), and 30 (*d*). (*c*) s_r and s_i for the same model but with $v = 40$ (*a*), 50 (*b*), 60 (*c*), and 70 (*d*).

where we have again assumed that $n = 1$. Unlike both equation (25) and the numerically determined values of s_r and s_i for $\kappa \ll 1$ (see Fig. 2*a*), an explicit dependence on κ is now apparent in equation (26). The physically relevant root of this quadratic equation is given approximately by

$$s \approx -\left(1 - \frac{\kappa v^{3/2}}{8\sqrt{2}}\right) + i\left(\frac{v}{4} - \frac{\kappa v^{3/2}}{8\sqrt{2}}\right), \qquad (27)$$

from which it is evident that for a prescribed value of v, s_r can be >0 for $\kappa > 8\sqrt{2}v^{-3/2}$. A proviso to this conclusion is that v must be large enough that $\kappa v^{3/2} > 8\sqrt{2}$ for κ sufficiently small that the approximations made in deriving equation (26) are valid. If this condition is fulfilled, the modes change from decaying to growing as κ increases, a transition that can be observed in the numerical results depicted in Figure 2. This behavior is a manifestation of the increasingly efficient operation of the dynamo for larger κ, a consequence of the growth of γ_0 implied by the assumed constancy of v. It is analogous to the change in the nature of the dynamo action that occurs for increasing α in kinematic models with uniform, constant values for η, α, and $\partial u/\partial z$ (see, e.g., Parker 1979; Stix 1989). Note also that according to equation (27), the change in the signature of s_r is accompanied by a steady decrease in the magnitude of s_i, a variation which is likewise visible in Figure 2.

Unlike most kinematic, mean-field, $\alpha\omega$-dynamos, in the model presently under consideration, the two inductive

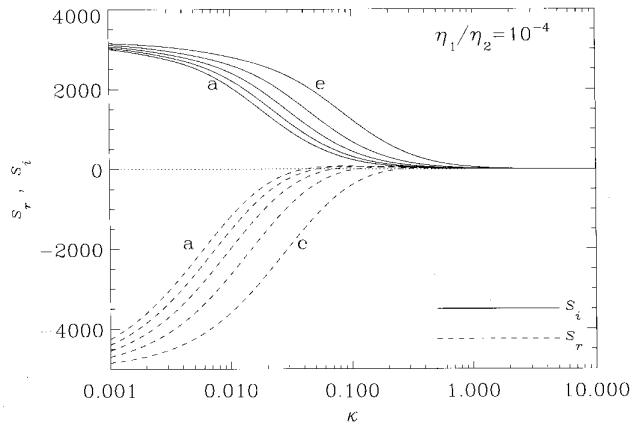

FIG. 4.—Quantities s_r and s_i as functions of κ for a dynamo model with $n = 10^{-4}$ and $v = 60$. The curves labeled a–e were obtained for $\Delta = 1.0$, 0.8, 0.6, 0.4, and 0.2, respectively.

components of the dynamo process are concentrated in two distinct, spatially separated layers. As a result of the assumed segregation of these physical effects, the mode of operation of the dynamo depends sensitively on the resistive diffusion of the fields between the adjacent source surfaces. Specifically, the y-directed field B produced by the shear layer at $z = 0$ must diffuse to the layer located at $z = d$ before the α-effect can contribute to the time and space evolution of the vector potential A. Similarly, the field A, once generated at $z = d$, can only act as the source of additional y-directed field B after diffusing to the site of the shear at $z = 0$. For larger values of κ, the finite time required for these fields to diffuse between the surfaces at $z = 0$ and d leads to the existence of modes with properties that are distinctly different from those associated with uniform, noninterfacial dynamos. This is apparent in Figure 2 where it can be seen that s_r, after increasing for $\kappa \approx 0.01$–0.1, decreases for $\kappa \gtrsim 1$. In particular, solutions with v large enough that positive growth occurs for intermediate values of κ are damped as the wave vector becomes large.

The origin of this behavior can be understood in the following way. Note that as the magnitude of κ increases, the horizontal wavelength of the corresponding dynamo wave decreases. Consequently, the x-components of the gradients of A and B increase, leading to a continuous decline in the time $(\eta_1 k^2)^{-1}$ required for resistive decay of a given mode. For a sufficiently small value of the horizontal wavelength, this dissipation timescale becomes equal to the diffusion time (d^2/η_1) between the layers at $z = 0$, d. All waves with shorter wavelengths damp faster than they can diffuse between the two source surfaces, each of which contains just one of the two inductive processes required to maintain the field. Hence, dynamo waves with $kd \gtrsim 1$ decay, regardless of the magnitudes of the α-effect and velocity shear. Such an inability to regenerate the field for large κ is a direct result of the assumed spatial separation of α and $\partial u/\partial z$.

When n has a value that differs from unity, many characteristics of the dynamo wave solutions are qualitatively similar to those noted in the preceding discussion. There are, however, a few significant exceptions. These are illustrated in Figure 3 where we depict the locus of roots s_r and s_i in the complex s-plane for a dynamo model with $n = 10^{-3}$ and $\Delta = 1$. In this representation, the value of κ increases continuously along each curve, from a starting value much less than 1 (usually $\kappa = 10^{-3}$) at the location marked by a triangle to an ending value much greater than 1 (usually $\kappa = 10$ to 10^2) in the vicinity of the branch point (indicated by a star) at $s = -1$. In so far as region (1) is intended to represent the stable, radiative layers just beneath the convection zone, we consider only models having $n < 1$ in order to simulate the turbulent enhancement of the diffusivity in region (2). As in Figure 2, the value of v is constant along each curve, with $v = 9$, 10, 11, 12 for cuves a–d in Figure 3*a*, $v = 15.16$, 20, 25, 30 in Figure 3*b*, and $v = 40$, 50, 60, 70 in Figure 3*c*. Unlike the results obtained when $n = 1$, for some values of v and $n < 1$, there exists a value of κ ($\geq 10^{-3}$) below which there are no solutions to the dynamo dispersion relation. The reason for this is evident in Figure 3*a*, wherein it can be seen that the long-wavelength end of the solution locus for each v value terminates in the branch cut along the negative real axis in the complex s-plane. For the results shown in the figure, the triangles that label the small-κ ends of the curves a–d correspond to solutions with $\kappa = 0.0099$, 0.0074, 0.0056, and 0.0042, respectively. Hence, along each locus, solutions for smaller κ values are contained on a different Riemann sheet, and are inaccessible to the present analysis. For $v > 15.16$, solutions exist for the entire κ range depicted (see Fig. 3*b*–3*c*), and bear a qualitative resemblance to the results shown in Figure 2. In particular, for v sufficiently large, wave growth only for κ in the finite range $0.01 \lesssim \kappa \lesssim 1$. Dynamo waves with shorter wavelengths are damped; indeed, for the frequencies and growth rates shown in Figure 3, $s_r \to -1$ and $s_i \to 0$ as κ becomes large, in agreement with the behavior displayed by the $n = 1$ results in the same limit.

Additional distinctions between dynamo solutions obtained for $n \ll 1$ and those corresponding to $n = 1$ can be seen by comparing the properties of the long-wavelength modes in Figures 2 and 3. Note that for $\kappa \ll 1$, the absolute magnitudes of s_r and s_i are significantly larger in the case of a dynamo with a nonuniform vertical distribution of magnetic diffusivity. As was true for the model having $n = 1$, approximate, analytic solutions to the dynamo dispersion relation can assist in the interpretation of this characteristic. When both κ and n are vanishingly small, equation (23) assumes the form

$$(1 + iv\kappa)ns^2 + [(1 + iv\kappa)^2 + 4inv]s + (1 + iv\kappa)^2 - (1 - iv)^2 = 0 . \quad (28)$$

In the limit $\kappa = 0$, the quadratic equation (28) has the particular solution

$$s = -\frac{1}{2n} + 2iv\left\{\left[1 + \frac{1}{4n} - \frac{1}{(4nv)^2}\right]^{1/2} - 1\right\}, \quad (29)$$

in which it has been assumed that v is large enough that the expression in brackets is positive. For values of v corresponding to the curves depicted in Figure 3*c*, equation (29) yields mode growth rates s_r and frequencies s_i that are in good agreement with computational results for $\kappa \lesssim 10^{-3}$.

Approximate solutions to the dynamo dispersion relation can also be obtained for the case in which $n = 0$. In this limit, the dispersion relation for $\kappa \ll 1$ follows directly from equation (28), and has the root

$$s = -1 + \frac{(1 - \kappa v^2)^2 - v^2(1 + \kappa)^2}{(1 + \kappa^2 v^2)^2} - i\,\frac{2v(1 + \kappa)(1 - \kappa v^2)}{(1 + \kappa^2 v^2)^2} . \quad (30)$$

As noted above, when n becomes small for κ large, s_r approaches the value -1, while s_i tends toward zero. An approximate dispersion relation for these short-wavelength modes can be derived from equation (23) with $n = 0$, and has the solution

$$s = -1 + \frac{1}{\kappa^2}\left[(\ln v)^2 - \frac{\pi^2}{4}\right] + i\,\frac{\pi}{\kappa^2}\ln v . \quad (31)$$

Thus far, we have considered only dynamo models for which the jump in the magnitude of the magnetic diffusivity occurs at the location of layer in which the α-effect is concentrated. In Figures 4 and 5, we examine how the properties of dynamo modes change as the transition between diffusivities is shifted within the interval $0 \leq z \leq d$. Because diffusion between the two surfaces is important to the overall operation of the dynamo, we anticipate that mode periods and growth/decay rates will change as the diffusi-

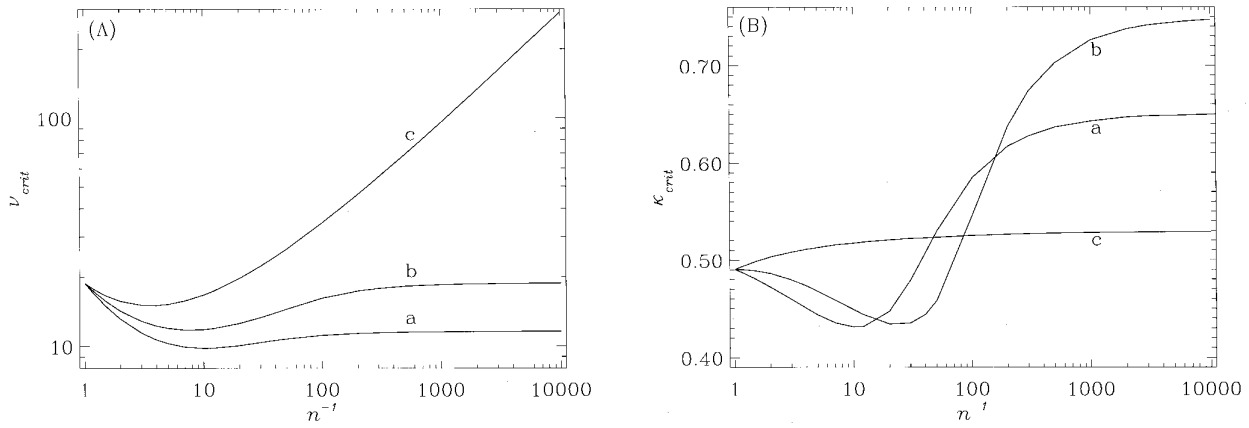

FIG. 5.—(*a*) Critical value of the dynamo number v (eq. [20]) as a function of the diffusivity ratio $n^{-1}(=\eta_2/\eta_1)$ for $\Delta = 1.0$ (*a*), 0.5 (*b*), and 0.0 (*c*). When $v = v_{crit}$, the single wave with horizontal wavenumber κ_{crit} has $s_r = 0$, while all others have $s_r < 0$. (*b*) Quantity κ_{crit} corresponding to the v_{crit} values of panel (*a*).

vity in this region varies between the values $\eta = \eta_1$ ($\Delta = 1$) and $\eta = \eta_2$ ($\Delta = 0$). This expectation is confirmed by the results shown in Figure 4, which were obtained for $n = 10^{-4}$. Unlike previous results, the curves labeled a–e in the figure all correspond to the same value of v (= 60), but have different Δ values (1.0, 0.8, 0.6, 0.4, and 0.2, respectively). Note that the dynamo period decreases (that is, s_i increases) as Δ is made smaller with κ held fixed. Not apparent in the figure is the fact that for the given values of n and v, each of the curves b–e terminates at a value of κ that decreases as Δ is made smaller. Specifically, solutions for $\Delta = 0.8$, 0.6, 0.4, and 0.2 cease to exist for κ greater than 20.42, 10.12, 6.61, and 4.73, respectively. As before, the reason for this behavior stems from the disappearance of each solution locus in the branch cut along the negative s_r-axis in the complex s-plane. When $\Delta = 0$, dynamo solutions terminate at $\kappa = 0.25$; all solutions for smaller values of κ decay at about the rate $s_r \approx -1/(2n)$ given by equation (29).

In Figures 5*a* and 5*b*, we show the values of v and κ corresponding to the first nondecaying modes of interface dynamo models with different magnetic diffusivity ratios. The results represented by the curves labeled a, b, and c were derived for $\Delta = 1.0$, 0.5, and 0.0, respectively. For a given model, the quantities v_{crit} and κ_{crit} characterize the single mode having $s_r = 0$; for $v = v_{crit}$, solutions of the dispersion relation for all other values of κ have $s_r < 0$. For $\Delta > 0$, v_{crit} and κ_{crit} are monotonic functions of n^{-1} $(=\eta_2/\eta_1)$, exhibiting a decrease for values of n^{-1} between about 1 and 10, and an increase as the ratio of magnetic diffusivities becomes larger. For $n^{-1} \gtrsim 10^3$, these quantities become nearly independent of the diffusivity ratio, with values $v_{crit} \approx 11.6$ and $\kappa_{crit} \approx 0.65$ for $\Delta = 1.0$, and $v_{crit} \approx 18.8$ and $\kappa_{crit} \approx 0.75$ for $\Delta = 0.5$. When $\Delta = 0$ (curve c), the dependences of v and κ_{crit} on n^{-1} are somewhat different from the results for $\Delta > 0$. For n^{-1} large, v_{crit} is strictly increasing (varying approximately as $n^{-0.5}$) over the range depicted, while κ_{crit} becomes nearly constant with value $\kappa_{crit} \approx 0.53$.

4. DYNAMO FIELDS

We complete our survey of interface dynamo properties by considering some of the physical characteristics of the generated fields. For this purpose, we choose a model with $n = 10^{-2}$, $\Delta = 1.0$, $v = 11.14$, and $\kappa = 0.586$. The dynamo waves obtained for these choices of input parameter values have $s_r = 3.142 \times 10^{-3}$ and $s_i = 6.687$, corresponding to a period $2\pi\omega^{-1} = 10.95$ (d^2/η_1) and a growth time $\sigma^{-1} = 3.707 \times 10^3$ (d^2/η_1). For this nearly steady solution of the dynamo dispersion relation, and the real and imaginary parts of the complex quantities v_1 $(\equiv q_1/k)$ and v_2 $(\equiv q_2/k)$ (see eqs. [21] and [B6]) have the values $v_{1r} = 1.97042$, $v_{1i} = 1.69688$, and $v_{2r} = 1.00057$, $v_{2i} = 0.03342$. Using this information together with the expressions given in Appendix B, the fields, A, B, B_x, and B_z can be evaluated as functions of x, z, and t.

Some of the results of this procedure are given in Figures 6 and 7, which show the dynamo fields as functions of z at $x = 0.0$, for a number of different times throughout the course of one period. The first panel in each figure depicts the fields at $x = 0.0$ and $z = 0.5$ d as functions of time; the solid dots therein denote the location in phase of the vertical profiles displayed in the subsequent panels. Figure 6 contains results pertaining to the time and space evolution of the vector potential and azimuthal magnetic field. Recall that the dynamo's operation depends, in part, upon the diffusive transport of the A and B fields between the source surfaces at $z = 0$ and $z = d$. Because of this, a time lag develops in the variation of A relative to that of B during the dynamo period, as examination of the panels reveals. In particular, note that the difference in phase between A and B is such that for the cycle depicted, the maximum and minimum values of B occur earlier in time (by an amount $\Delta t \approx d^2/\eta_1$) than do the corresponding maximum and minimum values of A. At any given time, the largest value of either field is found at the location of the relevant source surface, except during the time interval just before and after a sign reversal. Similar behavior can be seen in Figure 7, which shows an analogous time sequence of vertical profiles of the poloidal field components, B_x and B_z. Inspection of Figure 7*a* indicates that for the model presently under consideration, the poloidal magnetic components both lead the azimuthal field by a small amount in phase. Also evident in the figure is the discontinuity in B_x at the location $z = d$ of the α-effect, as dictated by equation (14b).

From Figure 6 it is further apparent that the magnitude of the azimuthal magnetic field in the region having high magnetic diffusivity ($z > d$) is significantly reduced in com-

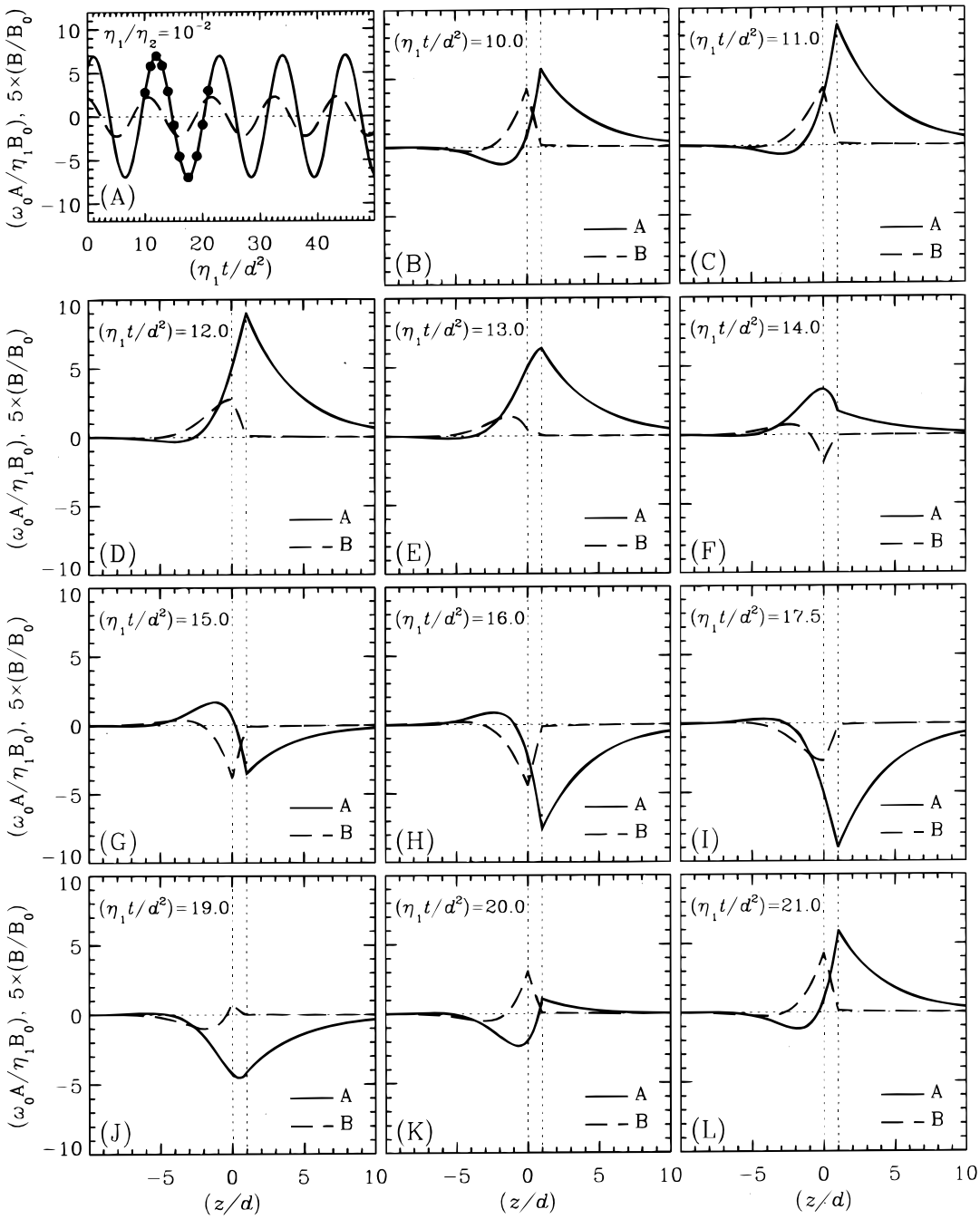

FIG. 6.—Fields A and B for $x = 0$ and $-10 \leq (z/d) \leq 10$ at a number of different times during the course of one period of a dynamo with $n = 10^{-2}$, $\Delta = 1$, $v = 11.14$, and $\kappa = 0.486$. The first panel of the figure depicts the fields at $x = 0$ and $(z/d) = 0.5$ as functions of time. The solid dots on the curve for A indicate the relative positions in phase of the vertical profiles shown in subsequent panels.

parison to that of the azimuthal field in the region with low magnetic diffusivity ($z < d$), where the BMRs are presumed to originate. Specifically, for the $n = 10^{-2}$ model described above, the maximum value of B in $z > d$ at any time during the cycle shown in Figure 6 is only about 3% of the corresponding maximum B value in $z < d$ over the same time interval. Such a disparity between the strengths of the azimuthal fields in different portions of the dynamo domain is also a feature of the interface dynamo model developed by Parker (1993).

This property is explored further in Figure 8, wherein we show the ratio $(B_{2,\max}/B_{1,\max})$ (the subscripts 1 and 2 denote the regions $z < d$ and $z \geq d$, respectively) as a function of η_2/η_1 $(=n^{-1})$ for both critical $(s_r = 0)$ and supercritical $(s_r > 0)$ dynamo solutions. The steady solutions are those whose dynamo numbers are depicted in Figure 5, while the growing solutions have $\Delta = 1$ and v chosen in such a way that for any n, the mode with the largest s_r value has a growth time $(\equiv \sigma^{-1})$ equal to the dynamo period. For comparison, we also show the n^{-1} dependence of the azimuthal field strength ratio derived by solving for the one-dimensional diffusion of a field in a composite medium, assuming that the value of the field on one boundary of the domain varies sinusoidally in time (see Appendix C for details). Given the one-dimensionality of this solution, its applicability as an interpretive tool is restricted to modes

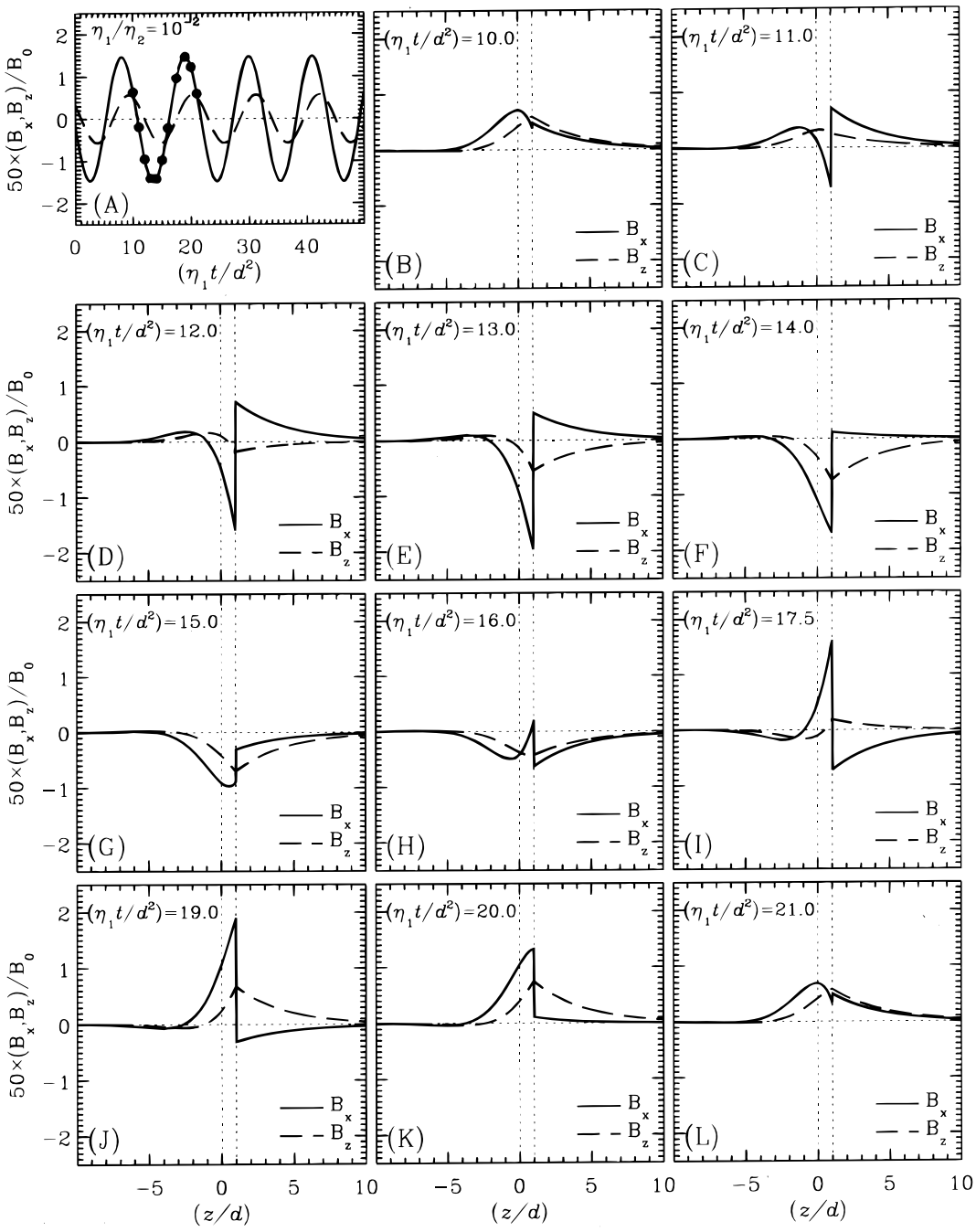

FIG. 7.—Time sequence of vertical profiles of the poloidal field components B_x and B_z for the dynamo wave solution of Fig. 8

having horizontal wavelengths that are sufficiently long that the timescale for diffusion in this (i.e., the x-) direction is longer than that for vertical (i.e., z-directed) diffusion.

As can be seen in Figure 8 and Appendix C, as the value of n becomes small, the ratio of maximum azimuthal field strengths obtained from the diffusion solution varies like $(\eta_2/\eta_1)^{-1/2} = n^{1/2}$. This is similar to the dependence found by Parker (1993), who studied the supercritical modes of a dynamo model in which the α-effect and the vertical shear are uniform within adjacent fluid layers having different magnetic diffusivities. In contrast, the ratio derived from consideration of the near-critical modes (i.e., $s_r \approx 0$) of the present dynamo model, while similar to that of the diffusion solution for $n^{-1} \lesssim 10$, exhibits a dependence on the diffusivity ratio that is closer to $(\eta_2/\eta_1)^{-1} = n$ for small values of n. The corresponding ratio in the case of the supercritical modes behaves in much the same way, except that the onset of an approximately linear dependence on n occurs for somewhat smaller values of n. Hence, the ratio $(B_{2,\max}/B_{1,\max})$ can be smaller for a model in which the shear and α-effect are spatially distinct yet individually localized than for one in which these processes are separate but uniformly distributed within their respective halves of the domain. We note that this conclusion has been arrived at by examining solutions obtained assuming $\Delta = 1$. If, for a given value of $n \ll 1$, Δ is made to approach zero, the magnitude of the ratio of maximum azimuthal field strengths increases. When $\Delta = 0$, the ratio becomes independent of n,

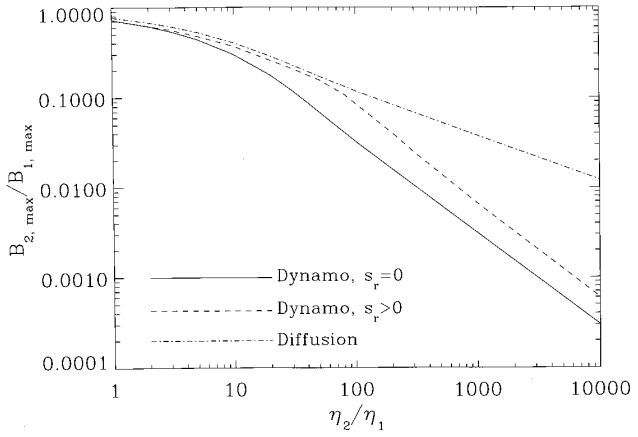

FIG. 8.—Azimuthal field strength ratio ($B_{2,\max}/B_{1,\max}$) as a function of η_2/η_1 for critical ($s_r = 0$) and super-critical ($s_r > 0$) dynamo solutions, as described in § 4 of the text. The solution to a problem describing the diffusion of a time-dependent field in a one-dimensional, composite medium is also shown for comparison.

with a value identical to that obtained in the absence of a discontinuity in the magnetic diffusivity (i.e., the case $n = 1$).

5. CONCLUSIONS AND DISCUSSION

We have examined the behavior of a simple, linear, kinematic dynamo model in which each of the two inductive components (i.e., the shear and α-effect) of the dynamo process is assumed to function by itself within a single, horizontal fluid layer. The dynamo is thus contained in two vertically separated layers, a spatial configuration which requires that the fields produced by each effect be transported between the sources surfaces by diffusion in order to complete one cycle of operation. It is this feature of the presumed dynamo structure that is responsible for the physical differences between the wavelike normal modes of the present model and those corresponding to either conventional $\alpha\omega$-type models or the interface dynamo described by Parker (1993). In light of recent helioseismic results suggesting the existence of a thin rotational shear layer located beneath the convection zone base, we feel that the model considered herein is perhaps a somewhat more realistic depiction of the actual environment of the solar dynamo. In an effort to achieve a degree of correspondence with the putative physical conditions that prevail at the base of the Sun's convection zone, the upper and lower portions of the dynamo domain are further characterized by different values of the magnetic diffusivity, reflecting the varying extent to which turbulent, convective motions can influence the magnitudes of transport coefficients in material located near the radiative-convective interface.

For any value of the diffusivity ratio n (< 1), it is possible to find growing wave solutions to the dynamo model described above, provided a suitably large value is assigned to the parameter v (see eq. [20]). However, unlike conventional kinematic $\alpha\omega$-type dynamos or the interface dynamo of Parker (1993), for fixed values of n, v, and the source surface separation d, growing modes are only obtained for a finite range of wavenumbers k. The existence of an upper limit to the range of wavenumbers for which positive growth of the wave amplitude can occur is a direct consequence of the fact that in the present model, the vertical shear and the α-effect are confined to distinct, nonoverlapping portions on the dynamo domain. An additional result of the assumed dynamo spatial structure is a reduction in the strength of the azimuthal field as the interface between low- and high-diffusivity regions is crossed. For both critical and super-critical dynamo modes, the magnitude of this reduction can be significant, varying nearly as n when the diffusivity jump occurs at the α-affect layer and the contrast between diffusivities is great. This behavior differs from that of the Parker (1993) model, in which the ratio of the strengths of the azimuthal fields on either side of the interface varies as $n^{1/2}$.

We conclude this section by attempting to ascertain how the interface dynamo model of the present paper might operate if it were to occupy the region immediately above and below the base of the solar convective envelope. Such an application is, of course, necessarily schematic, both because of the geometrical and physical shortcomings of the model itself and because of our ignorance concerning the magnitudes of the input parameters required to specify a solution. With these limitations in mind, we select input parameter values that yield a solution with characteristics that are similar to those of the example presented by Parker (1993). Specifically, we adopt $n = 10^{-2}$, $\Delta = 1$, $v = 120$, and chose the particular dynamo solution having $\kappa = 0.1349$, $s_r = 100.4$, and $s_i = 139.0$. To facilitate evaluation of further dynamo properties, we follow Parker (1993) and assume that the horizontal wavelength $2\pi k^{-1}$ of the mode is equal to the distance between the pole and the equator at the convection zone base, so that $k \approx 8 \times 10^{-11}$ cm^{-1}. This choice for k implies that the separation d between the source surfaces is $d \approx 0.012\ R_\odot$. Likewise, with $\eta_1 = 10^{10}$ cm^2 s^{-1} and $\eta_2 = 10^{12}$ cm^2 s^{-1}, it follows that the wave frequency is $\omega = \eta_1 k^2 s_i \approx 8.90 \times 10^{-9}$ s^{-1}, corresponding to a dynamo period $2\pi\omega^{-1} \approx 22.42$ yr. As in the case of the example discussed by Parker (1993), the dynamo wave is strongly supercritical, having an e-folding time $\sigma^{-1} = (\eta_1 k^2 s_i)^{-1} \approx$ 4.94 years.

For the solution presently under consideration, the quantities v_{1r} ($= q_{1r}/k$) and v_{2r} ($= q_{2r}/k$) have the values 11.69 and 1.49, respectively, so that the vertical scales of dynamo fields below and above the base of the convection zone are $q_{1r}^{-1} \approx 1.07 \times 10^9$ cm and $q_{2r}^{-1} \approx 8.39 \times 10^9$ cm. Furthermore, the maximum value of the azimuthal magnetic field B at the location of α-effect layer is about 0.105 times the maximum value of B at the location of the shear layer. The relative strengths of the processes that take place in these two layers are calibrated by the magnitude of the dynamo number v (see eq. [20]). For the assumed values of v, k, η_1, and η_2, the quantities ω_0 and γ_0 are related according to $(\omega_0 \gamma_0) = 4.848 \times 10^{15}$ cm^3 s^{-2}. Note that because we have chosen to represent the vertical distributions of the α-effect and fluid shear by δ-functions, the parameters ω_0 and γ_0 differ dimensionally from the analogous quantities G and Γ used in the formulation of Parker (1993). If we identify G with $(\omega_0\ k)$ and Γ with $(\gamma_0\ k)$, it follows that $(G\ \Gamma) = (\omega_0 \gamma_0\ k^2) = 3.103 \times 10^{-5}$ cm s^{-2}. Hence, for a vertical shear in the range $10^{-6} \leq G \leq 10^{-5}$ s^{-1}, the constraint provided by the dynamo number requires $31.0 \gtrsim \Gamma \gtrsim 3.1$ cm s^{-1}. These values are in reasonable agreement with the range of values inferred for Γ by applying conventional kinematic dynamo models to the interpretation of the solar cycle (see, e.g., Parker 1979).

The estimates of dynamo properties derived in the preceding paragraphs must, for reasons discussed earlier in this section, be regarded as an illustrative application of the

model rather than as a quantitatively reliable representation of the mechanism by means of which the Sun's magnetic field is generated. Subsequent papers in this series will take further steps toward a more realistic description of an interface dynamo, initially, through the inclusion of sphericity and solar-like internal differential rotation, and ultimately, by extending the model to incorporate non-linear effects.

We gratefully acknowledge discussions with Tom Bogdan and Graham Barnes concerning many aspects of the work described in this paper. We are also indebted to Tom Bogdan for his thorough examination of the manuscript, and to Jack Thomas and two anonymous referees for further comments on the first submitted version.

APPENDIX A

DERIVATION OF THE DYNAMO DISPERSION RELATION

In this appendix, we provide a more detailed description of the procedure used to derive the dispersion relation given in equation (19a). As is apparent from Figure 1 and equation (8), the dynamo domain is partitioned into two regions ($z < h$ and $z > h$), each characterized by a different value of the diffusivity η. The placement of the layers in which α and $\partial u/\partial z$ are nonzero (see Fig. 1 and eqs. [9] and [10]) has the effect of further subdividing these regions into lower (l) and upper (u) halves, hereafter denoted "$1l$" ($z < 0$), "$1u$" ($0 < z < h$), "$2l$" ($h < z < d$), and "$2u$" ($z > d$). Within each of these subdomains, the z-dependent portions of the solutions for A and B (see eqs. [16]–[18]) assume the form:

$$a_1(z) = a_{1l} \exp(q_1 z) , \tag{A1}$$

$$b_1(z) = b_{1l} \exp(q_1 z) , \tag{A2}$$

in $z < 0$,

$$a_1(z) = a_{1u} \exp(q_1 z) + a'_{1u} \exp(-q_1 z) , \tag{A3}$$

$$b_1(z) = b_{1u} \exp(q_1 z) + b'_{1u} \exp(-q_1 z) , \tag{A4}$$

in $0 < z < h$,

$$a_2(z) = a_{2l} \exp(q_2 z) + a'_{2l} \exp(-q_2 z) , \tag{A5}$$

$$b_2(z) = b_{2l} \exp(q_2 z) + b'_{2l} \exp(-q_2 z) , \tag{A6}$$

in $h < z < d$, and

$$a_2(z) = a_{2u} \exp(-q_2 z) , \tag{A7}$$

$$b_2(z) = b_{2u} \exp(-q_2 z) , \tag{A8}$$

in $z > d$.

The coefficients appearing on the right-hand side of equations (A1)–(A8) are complex constants whose values are determined by the requirement that the solutions satisfy the continuity conditions derived in § 2. At $z = 0$, application of conditions (11a) and (11b) yields

$$a_{1l} = a_{1u} , \tag{A9}$$

$$a'_{1u} = 0 , \tag{A10}$$

and

$$b_{1l} = b_{1u} + b'_{1u} , \tag{A11}$$

while condition (11c) (together with the second of conditions [11a]) implies that

$$a_{1u} = -\frac{2i\eta_1 q_1}{\omega_0 k} b'_{1u} . \tag{A12}$$

In a similar manner, continuity of A at $z = d$ leads to the result

$$a_{2u} = a_{2l} \exp(2q_2 d) + a'_{2l} , \tag{A13}$$

while the conditions governing the continuity of both B and $\partial B/\partial z$ (see eq. [15]) at that position provide the relations

$$b_{2l} = 0 , \tag{A14}$$

and

$$b'_{2l} = b_{2u} . \tag{A15}$$

Finally, from the conditions $[A] = [\partial A/\partial z] = 0$ at $z = h$, it follows that

$$a_{2l} = \left(\frac{q_1 + q_2}{2q_2}\right) \exp\,[(q_1 - q_2)h] a_{1u}\,, \tag{A16}$$

and

$$a'_{2l} = \left(\frac{q_2 - q_1}{2q_2}\right) \exp\,[(q_1 + q_2)h] a_{1u}\,, \tag{A17}$$

while imposition of the conditions $[B] = [\eta \partial B/\partial z] = 0$ (see eq. [13]) at the same location gives

$$b_{1u} = \left(\frac{\eta_1 q_1 - \eta_2 q_2}{\eta_1 q_1 + \eta_2 q_2}\right) \exp\,(-2q_1 h) b'_{1u}\,, \tag{A18}$$

and

$$b_{2u} = \left(\frac{2\eta_1 q_1}{\eta_1 q_1 + \eta_2 q_2}\right) \exp\,[(q_2 - q_1)h] b'_{1u}\,. \tag{A19}$$

Inspection of equations (A9)–(A19) reveals that all nonvanishing coefficients are expressible in terms of the single amplitude b'_{1u}. Moreover, note that there is one continuity condition which has yet to be enforced, namely,

$$2\eta_2 q_2 a_{2l} \exp\,(2q_2 d) = \gamma_0 b_{2u}\,, \tag{A20}$$

which follows from the use of the constraint (14a) at $z = d$. The dynamo dispersion relation given in equation (19) is obtained directly from equation (A20) by substituting equations (A16) and (A12) for a_{2l}, equation (A19) for b_{2u}, and simplifying the result.

APPENDIX B

DERIVATION OF THE DYNAMO FIELDS

In this appendix, we briefly describe the procedure used to assemble complete solutions for the fields A, B, B_x, and B_z as functions of space and time. We also provide explicit expressions for these quantities, valid within each of the four subdomains identified in Appendix A when $0 < h \leq d$.

To begin, note that the z-dependence of the A and B fields is given by equations (A1)–(A8) (see Appendix A), and that their x- and t-dependene is furnished by the common multiplicative factor $\exp\,[\sigma t + i(kx + \omega t)]$ (see eq. [16]). In addition, recall that the complex coefficients (see eqs. [A9]–[A19]) appearing in the solutions for A and B are all expressible in terms of the single magnetic field amplitude b'_{1u} ($\equiv B_0$, say). Hence, expressions for the dimensionless quantities

$$\hat{A} \equiv \frac{\omega_0 \mathrm{A}}{\eta_1 B_0} \qquad \text{and} \qquad \hat{B} \equiv \frac{B}{B_0}\,, \tag{B1}$$

can be constructed by forming the solutions appropriate to each subdomain in the manner described above, and taking the real parts of the results.

The poloidal magnetic field components, B_x and B_z, are evaluated by combining equation (4) with the definitions (B1) to obtain

$$\hat{B}_x \equiv \frac{B_x}{B_0} = -\frac{1}{R_\omega}\frac{\partial \hat{A}}{\partial \zeta} \qquad \text{and} \qquad \hat{B}_z \equiv \frac{B_z}{B_0} = \frac{1}{R_\omega}\frac{\partial \hat{A}}{\partial \xi}\,, \tag{B2}$$

where $\xi \equiv x/d$, $\zeta \equiv z/d$, and R_ω is the magnetic Reynolds number

$$R_\omega \equiv \frac{\omega_0 \mathrm{d}}{\eta_1}\,. \tag{B3}$$

Expressions for $\hat{B}_x$ and $\hat{B}_z$ then follow by performing the indicated differentiations of $\hat{A}$ and taking the real parts of the results. In order to assign a value to R_ω, we define a second magnetic Reynolds number

$$R_\alpha \equiv \frac{\gamma_0}{\eta_2}\,, \tag{B4}$$

and specify the magnitude of the ratio $\mu \equiv R_\alpha/R_\omega$. Then the product $R_\alpha R_\omega = \mu R_\omega^2 = (\kappa v/2n)$, and the Reynolds number R_ω can be expressed in terms of specified parameters as

$$R_\omega = \left(\frac{\kappa v}{2\mu n}\right)^{1/2}\,. \tag{B5}$$

The validity of mean-field electrodynamics that μ be $\ll 1$; to obtain the results discussed in § 4, we assumed $\mu = 10^{-2}$.

In the remainder of this Appendix, we give complete expressions for the scaled fields $\hat{A}$, $\hat{B}$, $\hat{B}_x$, and $\hat{B}_z$ throughout the dynamo domain. To facilitate the presentation of this material, we rewrite the complex quantities q_1 and q_2 (see eq. [21]) as

$$q_1 = k(1+s)^{1/2} = kv_1 \qquad \text{and} \qquad q_2 = k(1+ns)^{1/2} = kv_2 \,, \tag{B6}$$

and define the phase functions

$$\Phi_m = \Phi_{mr} + i\Phi_{mi} = (kv_{mr}z + \sigma t) + i(kv_{mi}z + kx + \omega t) \,, \tag{B7}$$

$$\Psi_m = \Psi_{mr} + i\Psi_{mi} = (-kv_{mr}z + \sigma t) + i(-kv_{mi}z + kx + \omega t) \,, \tag{B8}$$

where the index $m = 1, 2$. Then for $z < 0$ the fields are

$$\hat{A} = 2\exp(\Phi_{1r})[v_{1r}\sin(\Phi_{1i}) + v_{1i}\cos(\Phi_{1i})] \,, \tag{B9}$$

$$\hat{B} = \exp(\Phi_{1r})[(1+c_{1r})\cos(\Phi_{1i}) - c_{1i}\sin(\Phi_{1i})] \,, \tag{B10}$$

$$\hat{B}_z = \beta\exp(\Phi_{1r})[v_{1r}\cos(\Phi_{1i}) - v_{1i}\sin(\Phi_{1i})] \,, \tag{B11}$$

and

$$\hat{B}_x = \beta\exp(\Phi_{1r})[(v_{1r}^2 - v_{1i}^2)\cos(\Phi_{1i}) - 2v_{1r}v_{1i}\sin(\Phi_{1i})] \,, \tag{B12}$$

where $\beta = \kappa/R_\omega$. The complex constant $c_1 = c_{1r} + ic_{1i}$ appearing in equation (B10) is given by

$$c_{1r} = \exp(-\kappa v_{1r}\Delta)[u_{1r}\cos(\kappa v_{1i}\Delta) + u_{1i}\sin(\kappa v_{1i}\Delta)] \,, \tag{B13}$$

$$c_{1i} = \exp(-\kappa v_{1r}\Delta)[u_{1i}\cos(\kappa v_{1i}\Delta) - u_{1r}\sin(\kappa v_{1i}\Delta)] \,, \tag{B14}$$

with

$$u_{1r} = \frac{(nv_{1r} - v_{2r})(nv_{1r} + v_{2r}) - (nv_{1i} - v_{2i})(nv_{1i} + v_{2i})}{(nv_{1r} + v_{2r})^2 + (nv_{1i} + v_{2i})^2} \,, \tag{B15}$$

and

$$u_{1i} = \frac{(nv_{1i} - v_{2i})(nv_{1r} + v_{2r}) - (nv_{1r} - v_{2r})(nv_{1i} + v_{2i})}{(nv_{1r} + v_{2r})^2 + (nv_{1i} + v_{2i})^2} \,, \tag{B16}$$

In the region $0 < z \le h$, $\hat{A}$, $\hat{B}_x$, and $\hat{B}_z$ are still given by equations (B9), (B11), and (B12), respectively, while the expression for the azimuthal field becomes

$$\hat{B} = \exp(\Phi_{1r})[c_{1r}\cos(\Phi_{1i}) - c_{1i}\sin(\Phi_{1i})] + \exp(\Psi_{1r})\cos(\Psi_{1i}) \,, \tag{B17}$$

where c_1 is evaluated using equations (B13)–(B16).

For positions within the interval $h < z \le d$, the dynamo fields assume the forms

$$\hat{A} = \exp(\Phi_{2r})[c_{2r}\cos(\Phi_{2i}) - c_{2i}\sin(\Phi_{2i})] + \exp(\Psi_{2r})[c_{3r}\cos(\Psi_{2i}) - c_{3i}\sin(\Psi_{2i})] \,, \tag{B18}$$

$$\hat{B} = \exp(\Psi_{2r})[c_{4r}\cos(\Psi_{2i}) - c_{4i}\sin(\Psi_{2i})] \,, \tag{B19}$$

$$\hat{B} = -\frac{\beta}{2}\{(\exp(\Phi_{2r})[c_{2r}\sin(\Phi_{2i}) + c_{2i}\cos(\Phi_{2i})] + \exp(\Psi_{2r})[c_{3r}\sin(\Psi_{2i}) + c_{3i}\cos(\Psi_{2i})\} \,, \tag{B20}$$

and

$$\hat{B}_x = -\frac{\beta}{2}\{\exp(\Phi_{2r})[(v_{2r}c_{2r} - v_{2i}c_{2i})\cos(\Phi_{2i}) - (v_{2r}c_{2i} + v_{2i}c_{2r})\sin(\Phi_{2i})] - \exp(\Psi_{2r})$$
$$\times [(v_{2r}c_{3r} - v_{2i}c_{3i})\cos(\Psi_{2i}) - (v_{2r}c_{3i} + v_{2i}c_{3r})\sin(\Psi_{2i})]\} \,. \tag{B21}$$

In equations (B18)–(B21), the real and imaginary parts of the complex constants c_2, c_3, and c_4 are given by the following formulae:

$$c_{2r} = \exp\left[-\frac{\kappa}{2}(v_{2r} - v_{1r})\Delta\right]\left\{u_{2r}\cos\left[\frac{\kappa}{2}(v_{2i} - v_{1i})\Delta\right] + u_{2i}\sin\left[\frac{\kappa}{2}(v_{2i} - v_{1i})\Delta\right]\right\} \,, \tag{B22}$$

$$c_{2r} = \exp\left[-\frac{\kappa}{2}(v_{2r} - v_{1r})\Delta\right]\left\{u_{2i}\cos\left[\frac{\kappa}{2}(v_{2i} - v_{1i})\Delta\right] - u_{2r}\sin\left[\frac{\kappa}{2}(v_{2i} - v_{1i})\Delta\right]\right\} \,, \tag{B23}$$

with

$$u_{2r} = \frac{(v_{1r} + v_{2r})(v_{1i}v_{2r} - v_{1r}v_{2i}) + (v_{1i} + v_{2i})(v_{1r}v_{2r} + v_{1i}v_{2i})}{v_{2r}^2 + v_{2i}^2} \tag{B24}$$

and

$$u_{2i} = \frac{(v_{1i} + v_{2i})(v_{1i} v_{2r} - v_{1ir} v_{2i}) - (v_{1r} + v_{2r})(v_{1r} v_{2r} + v_{1i} v_{2i})}{v_{2r}^2 + v_{2i}^2} \tag{B25}$$

$$c_{3r} = \exp\left[\frac{\kappa}{2}(v_{1r} - v_{2r})\Delta\right]\left\{u_{3r}\cos\left[\frac{\kappa}{2}(v_{1i} - v_{2i})\Delta\right] - u_{3i}\sin\left[\frac{\kappa}{2}(v_{1i} + v_{2i})\Delta\right]\right\}, \tag{B26}$$

$$c_{3i} = \exp\left[\frac{\kappa}{2}(v_{1r} - v_{2r})\Delta\right]\left\{u_{3i}\cos\left[\frac{\kappa}{2}(v_{1i} - v_{2i})\Delta\right] + u_{3r}\sin\left[\frac{\kappa}{2}(v_{1i} + v_{2i})\Delta\right]\right\}, \tag{B27}$$

with

$$u_{3r} = \frac{(v_{2r} - v_{1r})(v_{1i} v_{2r} - v_{1r} v_{2i}) + (v_{2i} - v_{1i})(v_{1r} v_{2r} + v_{1i} v_{2i})}{v_{2r}^2 + v_{2i}^2} \tag{B28}$$

and

$$u_{3i} = \frac{(v_{2i} - v_{1i})(v_{1i} v_{2r} - v_{1r} v_{2i}) - (v_{2r} + v_{1r})(v_{1r} v_{2r} + v_{1i} v_{2i})}{v_{2r}^2 + v_{2i}^2} \tag{B29}$$

$$c_{4r} = \exp\left[\frac{\kappa}{2}(v_{2r} - v_{1r})\Delta\right]\left\{u_{4r}\cos\left[\frac{\kappa}{2}(v_{2i} - v_{1i})\Delta\right] - u_{4i}\sin\left[\frac{\kappa}{2}(v_{2i} - v_{1i})\Delta\right]\right\}, \tag{B30}$$

$$c_{4i} = \exp\left[\frac{\kappa}{2}(v_{2r} - v_{1r})\Delta\right]\left\{u_{4i}\cos\left[\frac{\kappa}{2}(v_{2i} - v_{1i})\Delta\right] + u_{4r}\sin\left[\frac{\kappa}{2}(v_{2i} - v_{1i})\Delta\right]\right\}, \tag{B31}$$

with

$$u_{4r} = 2n\left[\frac{v_{1r}(nv_{1r} + v_{2r}) + v_{1i}(nv_{1i} + v_{2i})}{(nv_{1r} + v_{2r})^2 + (nv_{1i} + v_{2i})^2}\right], \tag{B32}$$

and

$$u_{4i} = 2n\left[\frac{v_{1i}(nv_{1r} + v_{2r}) - v_{1r}(nv_{1i} + v_{2i})}{(nv_{1r} + v_{2r})^2 + (nv_{1i} + v_{2i})^2}\right]. \tag{B33}$$

Finally, within the region $z > d$, $\hat{B}$ is still given by equation (B19), while the expressions for $\hat{A}$, $\hat{B}_z$, and $\hat{B}_x$ become

$$\hat{A} = \exp(\Psi_{2r})[(c_{5r} + c_{3r})\cos(\Psi_{2i}) - (c_{5i} + c_{3i})\sin(\Psi_{2i})], \tag{B34}$$

$$\hat{B}_z = -\frac{\beta}{2}\exp(\Psi_{2r})[(c_{5i} + c_{3i})\cos(\Psi_{2i}) + (c_{5r} + c_{3r})\sin(\Psi_{2i})], \tag{B35}$$

and

$$\hat{B}_x = \frac{\beta}{2}\exp(\Psi_{2r})\{[v_{2r}(c_{5r} + c_{3r}) - v_{2i}(c_{5i} + c_{3i})]\cos(\Psi_{2i}) - [v_{2i}(c_{5r} + c_{3r}) + v_{2r}(c_{5i} + c_{3i})]\sin(\Psi_{2i})\}. \tag{B36}$$

In these expressions, the constant c_3 is computed according to equations (B26)–(B29), while

$$c_{5r} = \exp(\kappa v_{2r})[c_{2r}\cos(\kappa v_{2i}) - c_{2i}\sin(\kappa v_{2i})] \tag{B37}$$

and

$$c_{5i} = \exp(\kappa v_{2r})[c_{2i}\cos(\kappa v_{2i}) + c_{2r}\sin(\kappa v_{2i})] \tag{B38}$$

with c_2 given by equations (B22)–(B25).

APPENDIX C

DIFFUSION OF OSCILLATING FIELDS

We treat the following idealized problem pertaining to the diffusion of a magnetic field in a semi-infinite, composite medium. Consider the Cartesian domain $z \geq 0$ in which the region $0 \leq z \leq h$ contains material with magnetic diffusivity η_1, while the material in the region $z > h$ is characterized by the diffusivity η_2. At time $t = 0$, the y-directed magnetic field $B(z, 0)$ is assumed to vanish throughout the domain. For times $t > 0$, the field on the boundary at $z = 0$ is taken to vary in time as $B(0, t) = B_0 \cos \omega t$, where B_0 and ω are specified constants. For these boundary and initial conditions, we seek the solution $B(z, t)$ describing the diffusive transport of the field from $z = 0$ to any position within the domain.

At locations other than $z = h$, the field B satisfies the diffusion equation

$$\frac{\partial B}{\partial t} = \eta \frac{\partial^2 B}{\partial z^2}, \tag{C1}$$

where $\eta = \eta_1$ for $0 \leq z \leq h$ and $\eta = \eta_2$ for $z > h$. Because $\eta_1 \neq \eta_2$, the desired solution of equation (C1) is subject to the continuity conditions

$$[B] = 0 = \left[\eta \frac{\partial B}{\partial z}\right], \tag{C2}$$

at $z = h$ as discussed in § 2. Define the Laplace transform of B with respect to t according to

$$\tilde{B}(z, s) = \int_0^\infty dt\, e^{-st} B(z, t), \tag{C3}$$

where s is a complex number with a positive real part. As a function of s, $\tilde{B}$ satisfies the Laplace transform of equation (C1)

$$\frac{d^2\tilde{B}}{dz^2} = \frac{s}{\eta}\tilde{B}, \tag{C4}$$

and likewise obeys the transformed versions of the boundary and continuity conditions.

An acceptable solution to equation (C4) has the general form

$$\tilde{B}(z, s) = c_1 \exp\left[\sqrt{(s/\eta_1)}z\right] + c_2 \exp\left[-\sqrt{(s/\eta_1)}z\right], \tag{C5}$$

for $0 \leq z \leq h$ and

$$\tilde{B}(z, s) = c_3 \exp\left[-\sqrt{(s/\eta_2)}z\right], \tag{C6}$$

for $z > h$, where we have imposed the requirement that $\tilde{B}$ tend toward zero as z becomes large. The values of the constants c_1, c_2, and c_3 appearing in equations (C5) and (C6) follow from the application of the conditions (C2) and the boundary condition at $z = 0$. By utilizing the Laplace transforms of these constraints, we obtain

$$c_1 = -\frac{\epsilon s B_0}{s^2 + \omega^2} \frac{\exp\left[-2\sqrt{(s/\eta_1)}h\right]}{1 - \epsilon \exp\left[-2\sqrt{(s/\eta_1)}h\right]}, \tag{C7}$$

$$c_2 = \frac{sB_0}{s^2 + \omega^2} \frac{1}{1 - \epsilon \exp\left[-2\sqrt{(s/\eta_1)}h\right.}, \tag{C8}$$

and

$$c_3 = (1 - \epsilon) \frac{sB_0}{s^2 + \omega^2} \frac{\exp\left\{-\left[\sqrt{(s/\eta_1)} - \sqrt{(s/\eta_2)}\right]h\right\}}{1 - \epsilon \exp\left[-2\sqrt{(s/\eta_1)}h\right]}, \tag{C9}$$

where

$$\epsilon = \frac{1 - \sqrt{n}}{1 + \sqrt{n}}, \tag{C10}$$

with $n = (\eta_1/\eta_2)$. From these results, it is readily shown that $\tilde{B}(z, s)$ can be written as

$$\tilde{B}(z, s) = \frac{sB_0}{s^2 + \omega^2} \sum_{k=0}^{\infty} \epsilon^k \left\{\exp\left[-\sqrt{\frac{s}{\eta_1}}\Lambda_{1k}(z)\right] - \alpha \exp\left[-\sqrt{\frac{s}{\eta_1}}\Lambda_{2k}(z)\right]\right\}, \tag{C11}$$

for $0 \leq z \leq$ h and

$$\tilde{B}(z, s) = (1 - \epsilon) \frac{sB_0}{s^2 + \omega^2} \sum_{k=0}^{\infty} \epsilon^k \exp\left[-\sqrt{\frac{s}{\eta_1}}\Lambda_{3k}(z)\right], \tag{C12}$$

for $z > h$, where $\Lambda_{1k}(z) = (2kh + z)$, $\Lambda_{2k}(z) = [2(k + 1)h - z]$, and $\Lambda_{3k}(z) = [(2k + 1)h + (n)^{1/2}(z - h)]$.

The solution $B(z, t)$ is obtained by inverting the transforms given in equations (C11) and (C12). Apart from a multiplicative factor, the inversion of each term of the summations in expressions (C11) and (C12) for $\tilde{B}(z, s)$ contributes a term of the form (Erdelyi 1954)

$$\exp\left[-\sqrt{\omega\tau_{jk}(z)}\right] \cos\left[\omega t - \sqrt{\omega\tau_{jk}(z)}\right] - \frac{1}{\pi}\int_0^\infty du \frac{u \exp(-ut)}{u^2 + \omega^2} \sin\left[\sqrt{2u\tau_{jk}(z)}\right], \tag{C13}$$

in the corresponding summation for $B(z, t)$, where we have used the notation $\tau_{jk} = \Lambda_{jk}^2/(2\eta_1)$ with $j = 1, 2, 3$. We interpret the integral in (C13) as a transient arising from the impulsive turn-on of the system at $t = 0$. In the spirit of the derivation and

analysis of the dynamo dispersion relation given in preceding sections, we presume that its magnitude becomes small for times $t \gg \omega^{-1}$ and discard it. With this assumption the solution becomes

$$B(z, t) = B_0 \sum_{k=0}^{\infty} \epsilon^k \{\exp [-\sqrt{\omega\tau_{1k}(z)}] \cos [\omega t - \sqrt{\omega\tau_{1k}(z)}] - \epsilon \exp [-\sqrt{\omega\tau_{2k}(z)}] \cos [\omega t - \sqrt{\omega\tau_{2k}(z)}]\} , \quad \text{(C14)}$$

for $0 \leq z \leq h$ and

$$B(z, t) = (1 - \epsilon) B_0 \sum_{k=0}^{\infty} \epsilon^k \exp [-\sqrt{\omega\tau_{3k}(z)}] \cos [\omega t - \sqrt{\omega\tau_{3k}(z)}] , \quad \text{(C15)}$$

for $z > h$. Note that as n becomes vanishingly small, $\epsilon \to 0$ while $(1 - \epsilon) \to 2(n)^{1/2}$. Hence, we expect that for $n \ll 1$, the ratio $[B_{\max}(h, t)/B_{\max}(0, t)]$, where the subscript denotes the maximum value over the course of one period, should vary with n approximately like $(n)^{1/2}$.

REFERENCES

Brown, T. M., Christenson-Dalsgaard, J., Dziembowski, W. A., Goode, P., Gough, D. O., and Morrow, C. A. 1989, ApJ, 343, 526
Caligari, P., Moreno-Insertis, F., & Schüssler, M. 1995, ApJ, 441, 886
Charbonneau, P., Christensen-Dalsgaard, J., Henning, R., Schou, J., Thompson, M. J., & Tomczyk, S. 1997, in IAU Symp. 181, Sounding Solar and Stellar Interiors, ed. J. Provost, & F. X. Schmider (Dordrecht: Reidel), in press
Deinzer, W., & Stix, M. 1971, A&A, 12, 111
D'Silva, S. 1993, ApJ, 407, 385
D'Silva, S., & Choudhuri, A. R. 1993, A&A, 272, 621
D'Silva, S., & Howard, R. F. 1994, Sol. Phys., 151, 213
Erdelyi, A. 1954, Tables of Integral Transforms, Vol. 1 (New York: McGraw-Hill), 246
Fan, Y., & Fisher, G. H. 1996, Sol. Phys., 166, 17
Fan, Y., Fisher, G. H., & DeLuca, E. E., 1993, ApJ, 405, 390
Gilman, P. A., Morrow, C. A., & DeLuca, E. E. 1989, ApJ, 338, 528
Gough, D. O. 1991, in Angular Momentum Evolution of Young Stars, ed. S. Catalano & J. R. Stauffer (Dordrecht: Kluwer), 271
Kleeorin, N. I., & Ruzmaikin, A. A. 1981, Geophys. Astrophys. Fluid Dyn., 17, 281
Kosovichev, A. G. 1996, ApJ, 469, L61
Mathews, J., & Walker, R. L. 1970, Mathematical Methods of Physics (New York: Benjamin), 240
Moffatt, H. K. 1978, Magnetic Field Generation in Electrically Conducting Fluids (Cambridge: Cambridge Univ. Press), 197
Parker, E. N. 1975, ApJ, 198, 205
———. 1979, Cosmical Magnetic Fields (Oxford: Clarendon), 616
———. 1993, ApJ, 408, 707
———. 1994a, Spontaneous Current Sheets in Magnetic Fields (New York: Oxford Univ. Press)
———. 1994b, ApJ, 433, 867
Roberts, P. H. 1967, An Introduction to Magnetohydrodynamics (New York: American Elsevier)
Schüssler, M., Caligari, P., Ferriz-Mas, A., & Moreno-Insertis, F. 1994, A&A, 281, L69
Stix, M. 1989, The Sun (New York: Springer), 305
Stratton, J. A. 1941, Electromagnetic Theory (New York: McGraw Hill), 34
Tomczyk, S., Schou, J., & Thompson, M. J. 1995, ApJ, 448, L57